Periodico di Mineralogia ISSN: 0369-8963

## MULTI-MODAL FRAMEWORK FOR DISCRIMINATING WALRUS AND NARWHAL TUSKS VIA SPECTRAL AND MICROSTRUCTURAL SIGNATURES

Lu Xingyu<sup>1</sup> & Azimah Hussin<sup>2</sup>

Program Geologi, Jabatan Sains Bumi dan Alam Sekitar, Faculty of Science and Technology,

Universiti Kebangsaan Malaysia, 43600 UKM Bangi, Selangor Darul Ehsan, Malaysia

Corresponding author: p133528@siswa.ukm.edu.my

#### **Abstract**

A comprehensive multi-modal framework is developed for discrimination of narwhal and walrus tusks by integrating bulk chemistry (XRF), crystallography (XRD), micro geochemistry (SEM-EDX), molecular spectroscopy (Raman), and microtexture analysis (SEM/FFT). A curated set of 20 partial transverse sections (10 narwhal, 10 walrus) underwent standardized sample preparation and calibration protocols. Analytical outputs were converted into normalized, modality-specific scores and synthesized using a weighted multi-criteria decision analysis (MCDA), with optional Dempster-Shafer evidence aggregation to address missing or uncertain measurements. This methodology produces specimen-level classifications supported by explicit confidence metrics and a transparent evidence matrix. Findings indicate that a single bulk elemental ratio provides an effective primary screening parameter, while secondary indicators including layer-resolved crystallinity indices from XRD, Raman phosphate band metrics and amide signal visibility, and FFT-derived anisotropy facilitate resolution of borderline cases and identification of preservation status. The framework is minimally destructive, auditable, and adaptable for application in gemological, archaeological, and regulatory contexts. Emphasis on uncertainty management, incorporating borderline thresholds, conflict quantification, and escalation rules, ensures avoidance of overconfident assignments in compromised materials. This approach establishes a standardized and reproducible protocol for species attribution of marine ivory through accessible laboratory methods and interpretable data fusion.

Keywords: Marine ivory; Narwhal tusk discrimination; Walrus tusk identification; Marine ivory species attribution: Multi-modal analytical framework; Dempster–Shafer

Periodico di Mineralogia ISSN: 0369-8963

#### Introduction

Organic gemstones are gem materials composed of biological organic substances, including amber, pearls, and ivory. Among these, ivory holds significant historical and cultural importance, having been utilized for tools and ornamental objects since the Stone Age. Notably, the "Lion Man" ivory statue uncovered in Germany, dating back over 30,000 years, underscores ivory's unique cultural and anthropological significance (Tranchant et al., 2023). Walruses and narwhals, emblematic marine mammals of the Arctic, provide valuable sources of "marine ivory." Walruses, members of the pinniped family, possess prominent tusks in males often exceeding one meter, used primarily for support on ice and intra-species combat. Females also bear smaller tusks. Narwhals (Monodon monoceros), Arctic toothed whales, feature a single, elongated, spiraled tusk derived from the left maxillary tooth, reaching lengths of 2–3 meters. Recent quantitative analyses of the narwhal tusk spiral have determined an average spiral angle of approximately 66.90° relative to the tusk axis, highlighting its distinctive morphology (Kiladze & Chernova, 2018).

Historically, narwhal tusks were frequently mistaken for mythical "unicorn horns," prized among European royalty as miraculous cures and valued at times up to ten times the price of gold. Ancient Chinese texts document their use ground into medicinal powders intended for detoxification and protection from evil (Dasal et al., 2021). Walrus tusks held significant cultural importance among Arctic Indigenous communities, serving as materials for crafting artifacts and becoming prominent sources of ivory in medieval European trade. Despite their historical and cultural significance, walrus and narwhal tusks remain comparatively under-studied relative to terrestrial ivories such as those from elephants and mammoths. Terrestrial ivories have been extensively examined; diagnostic features such as Schreger line angles typically exceeding 100° in modern elephant ivory and less than 100° in mammoth ivory effectively facilitate species identification (Locke, 2008; Sims et al., 2011). Trace element profiles also distinguish these sources, with marine mammal ivory often containing fluoride concentrations in the thousands of ppm, whereas modern terrestrial ivory rarely exceeds a few hundred ppm. Consequently, elevated fluoride levels in ivory artifacts commonly indicate marine or fossil mammoth origin. However, systematic studies focusing on the mineralogy, microstructure, and geochemistry of walrus and narwhal tusks are scarce, limiting the development of robust and reliable identification frameworks.

Mineralogical and geochemical methodologies have proven invaluable in studying organic gem materials and ivory artifacts (Sastri et al., 2013). Analytical techniques such as X-ray diffraction (XRD) and infrared spectroscopy have been widely applied to elucidate the mineralogical and chemical compositions of these materials, revealing microstructural characteristics and their evolutionary pathways. For instance, infrared spectroscopy has been successfully employed to examine amber and mammoth ivory, identifying key components including structural water, collagen proteins, and hydroxyapatite. Moreover, portable X-ray fluorescence (XRF) spectrometry has gained prominence as a rapid, non-destructive onsite method for identifying ivory types. Determination of elemental ratios, particularly calcium-to-phosphorus (Ca/P), has significantly improved the accuracy of ivory source differentiation, proving essential in combating illegal ivory trade (Lambert & Poinar, 2002; McLellan et al., 2022a).

ISSN: @662-8666plexity of the global ivory trade, encompassing multiple species and regulated under CITES, underscores the need for dependable and non-destructive methods for source attribution. Both gemological and heritage conservation fields require accurate species identification to establish authenticity and provenance. Nonetheless, reliable non-destructive identification remains challenging: texture-based discrimination often necessitates invasive sampling, while spectroscopic approaches, including Raman spectroscopy, face limitations from fluorescence and sample degradation in archaeological specimens (Edwards & O'Connor, 2012). A notable case involving Anglo-Saxon ivory rings demonstrated these difficulties, as extensive multi-modal analysis was required to conclusively attribute the artifacts to African elephant ivory, rather than walrus or mammoth sources. Such examples highlight the critical need for focused research on marine ivories to illuminate ancient trade networks and enhance contemporary forensic efforts. Therefore, advancing the mineralogical and geochemical understanding of walrus and narwhal tusks holds substantial scientific and practical significance (Hemer et al., 2023).

To address these gaps, this study proposes a multi-modal analytical framework for discriminating walrus and narwhal tusks. The framework integrates complementary analytical techniques—including X-ray fluorescence (XRF), X-ray diffraction (XRD), Raman spectroscopy, scanning electron microscopy (SEM), and energy-dispersive X-ray spectroscopy (EDX)—to capture elemental composition, crystallinity, molecular vibrations, and microstructural anisotropy. We propose a unified decision-making protocol to organize these multidimensional data into a structured, interpretable classification scheme. The workflow begins with primary screening based on bulk elemental ratios derived from XRF. When ambiguity arises due to preservation or compositional overlap, additional parameters such as crystallinity indices, Raman spectral features, and SEM-derived textural orientation metrics are incorporated. Each modality is normalized and integrated within a multicriteria decision analysis (MCDA) model, optionally supplemented by evidence fusion using Dempster–Shafer theory to manage uncertainty and incomplete data (Xiao, 2017). This approach facilitates transparent, repeatable, and minimally invasive specimen-level assessments, rendering it suitable for applications in gemology, archaeology, and regulatory enforcement.

## **Materials and Methods**

A multi-technique analytical approach was employed to compare narwhal and walrus tusk specimens. Twenty partial transverse sections were analyzed, comprising ten narwhal (N1–N10) and ten walrus (W1–W10) samples. All specimens were legally sourced as by-products of traditional subsistence hunting by indigenous communities in the Russian Far East and originated from historical stockpiles held under international cultural-use exemptions. Representative samples are illustrated in Figure 1. Comprehensive characterization was conducted at the Institute of Climate Change Research and Innovation Materials (ICRIM) Laboratory, Universiti Kebangsaan Malaysia (UKM). The analytical techniques applied included Field Emission Scanning Electron Microscopy coupled with Energy-Dispersive X-ray Spectroscopy (FESEM-EDAX), X-ray Diffraction (XRD), X-ray Fluorescence (XRF), and Raman Spectroscopy.

Field Emission Scanning Electron Microscopy coupled with Energy-Dispersive X-ray Spectroscopy (FESEM-EDAX) was employed for microstructural and elemental characterization. Specimens were carbon-coated to minimize charging artifacts, with imaging conducted at pagagnifications ranging from 2,000× to 10,000× to document dentipal/microstructureser/EDAX/481188

ISANI 9369 were performed in both point and area modes, calibrated and optimized to enable quantitative assessment of key elemental distributions. X-ray Diffraction (XRD) analysis was conducted for crystalline phase identification. Samples were pulverized to particle sizes below 74 μm and scanned over a 2θ range of 5° to 60° using standardized operating parameters. Phase identification was achieved by matching diffraction patterns against reference databases within the International Centre for Diffraction Data Powder Diffraction File (ICDD PDF-4+), facilitating accurate mineralogical characterization.

Bulk chemical composition was determined by X-ray fluorescence (XRF) analysis performed on pressed powder pellets. Calibration was carried out using certified reference materials to ensure analytical accuracy. A helium purge was applied to enhance sensitivity for light element detection, achieving detection limits on the order of approximately 15 ppm. Raman spectroscopy was conducted utilizing a 532 nm excitation laser, with the beam focused to an approximate spot size of 1 µm. Spectral acquisition covered the range of 200 to 3,200 cm<sup>-1</sup>, and subsequent data processing enabled high-resolution extraction of molecular vibrational signatures and crystallographic phase information. Post-acquisition, all analytical data were compiled into a structured dataset for comparative analysis. Specimen classification into walrus or narwhal origin was performed through a multi-criteria decision analysis (MCDA) framework. Key analytical parameters including elemental ratios derived from XRF and EDAX, crystallinity indices from XRD, molecular vibrational characteristics from Raman spectra, and microtextural orientation metrics from SEM imaging were extracted and subjected to range normalization to preserve relative variability and mitigate the influence of outlier values. Each normalized feature was assigned a walrus-leaning score quantifying the degree of correspondence with walrus tusk characteristics.

The final classification score, designated as the composite walrus index, was calculated as a weighted sum of all normalized modality-specific scores. Weights were assigned according to the relative diagnostic strength and robustness of each parameter. Specimens with scores near the decision threshold (e.g., S∈[0.45,0.55]) or exhibiting preservation-related artifacts were flagged for further evaluation. In instances of incomplete or ambiguous data, Dempster–Shafer evidence theory was employed to perform conservative evidence fusion by assigning basic probability masses to each modality and combining them to generate belief and plausibility measures. This dual approach facilitated explicit treatment of uncertainty and conflict within the classification process. Results were documented in a specimen-level evidence matrix, enabling transparent reporting and traceability of the rationale underpinning each classification outcome.

## **Results and Discussion**

This section presents and interprets the results obtained from X-ray Diffraction (XRD), X-ray Fluorescence (XRF), Scanning Electron Microscopy coupled with Energy Dispersive X-ray Spectroscopy (SEM-EDX), and Raman spectroscopy analyses performed on walrus and narwhal tusk specimens. Comparative evaluation of mineralogical, geochemical, and microstructural signatures facilitates identification of distinguishing characteristics and commonalities between the two species

#### Pre-analytical data preparation XRF and EDX results.

This study employed elemental concentration heatmaps derived from X-ray fluorescence (XRF) data alongside scanning electron microscopy with energy-dispersive X-ray spectroscopy (SEM-EDX) to compare and discriminate walrus and narwhal tusks. The heatmaps provided intuitive visualizations of elemental distributions, while SEM-EDX offered detailed, spot-specific elemental profiles. These Passalbined data are summarized in Table 1 for direct comparison. Boths: Walrus 241052241 (2016)

ISSA in 1879 8963 sist of hydroxyapatite, with calcium oxide (CaO) content ranging approximately between 60–62% and phosphorus pentoxide (P<sub>2</sub>O<sub>5</sub>) content between 33–34%. Narwhal tusks slightly exceed walrus tusks in P<sub>2</sub>O<sub>5</sub> content (33.86% vs. 32.87%), whereas walrus tusks have marginally higher CaO levels (61.71% vs. 60.66%). Additionally, walrus tusks display elevated concentrations of sodium oxide (Na<sub>2</sub>O), magnesium oxide (MgO), strontium oxide (SrO), aluminum oxide (Al<sub>2</sub>O<sub>3</sub>), and silicon dioxide (SiO<sub>2</sub>), suggesting a more complex mineral incorporation or post-depositional alteration compared to narwhal tusks. This compositional heterogeneity likely reflects differences in biological formation and environmental exposure between the two species.

Sulfur trioxide (SO<sub>3</sub>) content is notably higher in walrus tusks (0.99%) compared to narwhal tusks (0.348%), whereas chloride (Cl) levels display the opposite trend, being lower in walrus tusks. These variations are consistent with distinct habitat conditions and diagenetic histories influencing mineral composition (Hoelzig et al., 2020; Nganvongpanit, Buddhachat, Klinhom, et al., 2016). Zinc oxide (ZnO) concentrations are low but slightly elevated and more variable in walrus tusks (0.104%) than in narwhal tusks. Overall, walrus tusks exhibit higher and more variable alkali metal oxides, trace impurities, and sulfate levels, indicative of a more heterogeneous mineralogical structure and depositional history. In contrast, narwhal tusks present a relatively uniform Ca-P matrix, making them a useful reference for hydroxyapatite purity.

Previous studies have validated the use of handheld XRF spectrometry specifically the Olympus Vanta M-series in Geochem2 mode with dual 10-second scans per sample surface (5 s high-energy + 5 s low-energy) to quantify weight percentages of Ca, P, and light elements (atomic number < 12). This approach successfully differentiates non-ivory biominerals such as deer bone and antler from genuine ivory (Nganvongpanit, Buddhachat, Piboon, et al., 2016; McLellan et al., 2022b). SEM-EDX analyses further complement these results, showing that walrus tusks are enriched in magnesium (~0.8 wt %) compared to narwhal tusks (~0.5 wt %). Sodium content is slightly higher in narwhal tusks (1.0 wt %) than in walrus tusks (0.8 wt %), though this overlap limits its discriminatory power. Major elements such as oxygen, carbon, calcium, phosphorus, and chlorine are comparable between species, with Ca/P molar ratios consistently between 1.92 and 1.96, rendering them ineffective for specieslevel differentiation. Nonetheless, EDX remains a valid supporting technique for elemental characterization.

Building on elemental data, a robust discrimination strategy is proposed based on the aluminumto-phosphorus oxide ratio (Al<sub>2</sub>O<sub>3</sub>/P<sub>2</sub>O<sub>5</sub>). Within the dataset, this ratio ranges from 0.00057 to 0.00322 in narwhal tusks, whereas walrus tusks exhibit higher values, ranging from 0.00333 to 0.03445. By establishing a threshold ratio R0=0.0033, specimens with R<R0 are classified as narwhal tusks, while those with R>R0 are classified as walrus tusks. Notably, no overlap occurs at this threshold in the sample set, resulting in zero classification errors: all narwhal tusks fall below 0.0033, and all walrus tusks exceed this value. Additionally, magnesium-to-sodium ratios derived from SEM-EDX data provide a supplementary discrimination parameter. Using a threshold R2≈0.75, samples with R2<0.75 correspond to narwhal tusks, and those with R2>0.75 correspond to walrus tusks. However, due to the smaller sample size and some overlap observed with this ratio, it is recommended as an auxiliary indicator rather than a primary discriminator. In summary, the Al<sub>2</sub>O<sub>3</sub>/P<sub>2</sub>O<sub>5</sub> ratio offers a highly reliable and straightforward metric for differentiating narwhal and walrus tusks based on elemental compositions obtained via XRF, supported by SEM-EDX characterization. This method serves as an effective pre-analytical screening tool, reducing the need for destructive testing and

ISSN: 0369-8963

## The SEM and Raman Spectrometer results

Scanning electron microscopy (SEM) images and Raman spectra provide localized surface information at micro- to nanometer scales, revealing morphology, pore structure, and chemical bonding characteristics. In this study, SEM images were obtained for samples from groups N6 and W9, with representative micrographs presented in the figures. The integration of morphological and chemical data from specific sample locations improves the accuracy of interpretation. Sample N6 (narwhal tusk) displays a well-preserved fibrous—crystalline structure characterized by uniform hydroxyapatite crystals aligned along collagen fibers, smooth surfaces, and fine pores, indicative of intact organic and mineral phases. In contrast, sample W9 (walrus tusk) shows evidence of collagen degradation, the presence of crystalline aggregates, macropores, cracks, and secondary precipitates, suggesting processes of weathering, dissolution, and recrystallization that lead to compromised structural integrity and disrupted crystal organization (Engel et al., 2022; Unal et al., 2021; Xiang et al., 2024).

These microstructural variations observed in the SEM images highlight the contrast between the highly crystalline, well-ordered calcium phosphate—organic composite framework of the narwhal tusk and the disrupted structure of the walrus tusk. Representative SEM images were selected for texture orientation analysis using Fourier Transform (FFT) and Gabor filtering. The 2D FFT decomposes grayscale SEM micrographs I(x,y) into spatial frequencies F(u,v), revealing periodic structures (e.g., tubules, lamellae) as streaks or spots perpendicular to their real-space orientation. The magnitude spectrum F(u,v) reflects structural strength, while the angular distribution encodes anisotropy. In this study, FFT was used to highlight microstructural differences between narwhal and walrus tusks. The central frequency region represents large-scale dentin homogeneity, while peripheral high frequencies reflect fine features like tubules. Directional tubules in narwhal tusks yield clear, perpendicular spectral streaks, indicating strong anisotropy. In contrast, walrus dentin shows denser, isotropic textures with uniform spectra lacking distinct peaks. Thus, anisotropic features (e.g., radial tubules) produce sharp, directional signatures in the Fourier domain, whereas isotropic or compact structures yield diffuse, non-directional distributions as shown in Figure 6.

The narwhal specimen (N6-03) displayed distinct directional streaks in the frequency domain, reflecting significant anisotropy consistent with the radial arrangement of dentinal tubules. Its Gabor filter responses were enhanced at approximately 0°/180° and ~90°, confirming the presence of highly repetitive tubular structures and organized alignment. By contrast, the walrus specimen (W9-03) showed a more uniform spectral distribution with clear isotropic features, lacking pronounced directional streaks. Its Gabor responses fluctuated more markedly across angles, with a notable decline near 90°, resulting in an irregular pattern indicative of a compact and homogeneous microstructure rather than a strongly oriented tubular arrangement. (Kinney et al., 1999; Manjunath, 1996; Nazhvani, 2019). Narwhal dentin exhibits pronounced textural anisotropy resulting from the alignment of dentinal tubules, whereas walrus dentin tends toward isotropy, characterized by a denser and more homogeneous microstructure at the microscale. This texture orientation analysis quantitatively supports the species-level differences inferred from SEM morphological observations.

Representative samples N4 and W10 were selected for Raman spectroscopic analysis to facilitate

Patrocal Comparison. The Raman spectra of both samples are presented to get their are a comparison. The Raman spectra of both samples are presented to get their are a comparison.

ISSNability-Steafer correlation between morphological features and characteristic vibrational peaks (Figures 6 and 7). The right panel of Figure 7, showing the Raman spectrum of sample W10, serves as the primary reference for discussion and its correlation with SEM imagery. Several prominent absorption peaks are observed: bands at 411 cm<sup>-1</sup> and 617 cm<sup>-1</sup> correspond to the v<sub>2</sub> and v<sub>4</sub> bending modes of the PO<sub>4</sub><sup>3-</sup> group, indicative of a hydroxyapatite lattice structure (Unal et al., 2021). The 871 cm<sup>-1</sup> peak is attributed to the v<sub>2</sub> deformation vibration of B-type substituted CO<sub>3</sub><sup>2-</sup>, implying carbonate substitution within the hydroxyapatite lattice. The 961 cm<sup>-1</sup> peak, representing the v<sub>1</sub> symmetric stretching vibration of PO<sub>4</sub><sup>3-</sup>, is the primary characteristic peak of hydroxyapatite; its sharpness reflects mineral crystallinity. A weak peak near 1317 cm<sup>-1</sup> is assigned to CH<sub>2</sub> side-chain twisting in collagen or the Amide III region, while the 1608 cm<sup>-1</sup> peak corresponds to the C=O stretching vibration in the Amide I region, confirming the residual presence of organic collagen matrix (Morris & Mandair, 2011). Collectively, these features suggest the sample comprises a composite of highly crystalline hydroxyapatite and organic collagen matrix. Differences between N4 (red) and W10 (blue) are evident in Figure 7 (left) and Raman spectra in Figure 8. The 961 cm<sup>-1</sup> PO<sub>4</sub><sup>3-</sup> peak is sharper and more intense (~80 counts) in N4 than in W10 (~25 counts), indicating higher hydroxyapatite crystallinity in the narwhal tusk. Furthermore, amide bands at 1249, 1443, and 1664 cm<sup>-1</sup> appear in N4 but are nearly absent in W10, consistent with organic matrix loss or masking by secondary mineralization, corroborating SEM evidence of surface weathering and mineral reprecipitation in W10.

#### The XRD Results

The X-ray diffraction (XRD) analysis was systematically performed on all specimens, encompassing narwhal (N1–N9) and walrus (W1–W10) tusks, revealing a predominant chemical similarity across samples. Representative diffraction patterns from samples N6 and W9 exhibited the characteristic reflections of apatite, albeit with slight peak shifts and additional peaks attributable to elemental substitutions, primarily carbonate and fluoride ions. These variations correspond to differences in ion incorporation and crystallinity, thereby offering valuable insights into the biomineralization processes and the influence of environmental factors. Simplified diffraction profiles emphasized the core apatite framework alongside subtle structural variations, facilitating comparative analysis of crystallographic features between the two species. Notably, XRD patterns confirmed calcium phosphate as the principal constituent, predominantly in the form of hydroxyapatite. Variations in peak positions, particularly minor shifts around 30–33° 20 and the presence of weak carbonate-related peaks, suggested the substitution of carbonate ions within the hydroxyapatite lattice, resulting in carbonate-hydroxyapatite. Some samples also indicated fluoride substitution, evidenced by intensified peaks near 26°, consistent with the presence of fluorapatite, known to enhance crystallinity (Madupalli et

ISSN: 0 160 167 163 whal and walrus tusks exhibited similar primary XRD peaks indicative of a hexagonal apatite structure, with minor distinctions in peak intensities and subtle details. Variations near the (211)/(112) reflections at approximately 31° 2θ implied differences in ionic substitution or impurity levels. Certain narwhal samples demonstrated higher-intensity peaks shifted marginally to higher angles, suggestive of lattice contraction likely induced by increased carbonate incorporation, which typically decreases the lattice parameter along the a-axis. Carbonate-apatite was present in both tusks, with approximately 40% carbonate content in samples W2 and N2, significantly impacting peak positions and intensities. Broad diffraction peaks accompanied by elevated background signals illustrated the presence of nanoscale, poorly crystalline bioapatite. Whereas walrus tusks displayed sharper peaks and larger crystallite sizes, narwhal tusks manifested broader, more disordered crystals, possibly reflecting biological function diversity or differential preservation states.

Impurity atom incorporation into apatite structures was evident, with antimony (Sb) and cadmium (Cd) uniquely detected in narwhal tusks for example, sample N1 exhibited about half the XRD intensity attributable to Sb-substituted apatite phases, while sample N2 showed clear Cd-substituted apatite signatures. Conversely, walrus tusks demonstrated significant vanadium (V) doping, with sample W1 presenting prominent reflections corresponding to V-substituted apatite. Both ivory types also showed substitutions involving strontium (Sr), sodium (Na), and magnesium (Mg) cations, implying environmental and dietary influences on elemental composition (Etcheverry et al., n.d.; Smičiklas et al., 2010). The detection of impurity elements such as Sb, Cd, and V provides geochemical markers reflecting provenance, environmental exposure, and feeding ecology. While apatite remains the dominant mineral phase, crystallinity variations assessed through crystallinity index (CI) calculations derived from XRD profiles highlighted differences linked to anatomical layers and preservation conditions, which impacts crystal growth and structural order. These findings collectively advance understanding of subtle biomineral variations arising primarily from biological and possibly environmental factors, with limited diagenetic alteration

The crystallinity index (CI) has been widely employed as a relative measure of lattice order in biological apatites. The most commonly applied definition is that proposed by Person et al. (1975), later adopted and refined in archaeological and geochemical studies (e.g., Shemesh, 1990). According to this method, CI is expressed as:

$$CI = \frac{I_{300}}{V_{112/300}}$$

where  $I_{300}$  represents the peak intensity of the (300) reflection at  $\sim 32.9^{\circ}$  20, and  $V_{112/300}$  is the minimum intensity in the valley between the (112) and (300) reflections. A higher CI value indicates Page 230 https://doi.org/10.5281/zenodo.17481188

ISSNair@669d8063ction peaks and deeper inter-peak valleys, corresponding to a higher degree of crystallinity and lattice ordering. Typical CI values for fresh biological teeth and bones fall in the range of 2–5, whereas heavily mineralized or heat-treated specimens can exceed 6–8. This parameter is therefore widely used in bioarchaeology, forensic sciences, and diagenetic studies as a convenient indicator of apatite preservation and post-depositional alteration.(Person et al., 1995). Using the defined method, the crystallinity index (CI) was calculated for all narwhal (N1–N9) and walrus (W1–W9) tusk specimens based on XRD profiles, specifically from the (300) peak intensity and interpeak valley between (112) and (300) reflections. The resulting CI values are summarized in Table 3. CI is known to vary with tissue type, species, and preservation state: modern bone and teeth typically show CI values between 2.0–3.5, while archaeological or heat-altered samples may exceed 5.0–6.0.

Narwhal tusks exhibit tightly clustered crystallinity index (CI) values averaging approximately  $2.06 \pm 0.24$ , with notably higher crystallinity observed in the inner dentin regions. In contrast, walrus tusks demonstrate a bimodal CI distribution, reflecting structural heterogeneity between anatomical layers. These patterns reaffirm apatite as the principal mineral phase and underscore the substantial influence of sampling depth and environmental exposure on mineral preservation and structural organization. The CI thus constitutes a robust parameter for distinguishing species origin and assessing preservation status, particularly when integrated with complementary analytical techniques. This study integrates five complementary modalities SEM/FESEM for microtexture and anisotropy analysis, EDX for localized elemental quantification (notably Mg, Na, and Ca/P ratios), XRF for bulk oxide compositions and elemental ratios, XRD for assessing crystallinity via Pearson's CI, and Raman spectroscopy for characterizing apatite and organic matrix vibrational bands within a single, auditable framework. Empirically, bulk XRF elemental ratios provide a clear distinction between narwhal and walrus classes, with secondary ratios offering informative insights near classification boundaries. XRD data reveal a tight CI distribution in narwhal tusks versus a bimodal pattern in walrus specimens, where higher CI is typically associated with inner dentin and lower CI with cortical regions. Raman spectroscopy further corroborates this differentiation, as narwhal exemplars feature sharper hydroxyapatite peaks and discernible amide bands indicative of residual organic matrices. SEM combined with FFT analysis evidences stronger directional anisotropy in narwhal tusks, consistent with organized tubular microstructures, whereas walrus tusks exhibit more isotropic, compact textures.

Collectively, the convergence of these multi-technique analytical data provides a powerful approach for species-level discrimination, mineralogical characterization, and evaluation of preservation states in tusk biominerals. The crystallinity index, encompassing the influence of anatomical variation and environmental effects, emerges as a particularly valuable quantitative indicator within this integrative analytical platform.

Periodico di Mineralogia ISSN: 0369-8963

## **Structured Decision Pathway**

The classification and interpretation of tusk samples rely on the integration of multiple complementary analytical techniques. To ensure consistent, transparent, and robust decision-making, a structured pathway was developed. This decision framework sequentially applies primary screening, condition checks, secondary evaluations, and composite scoring to address preservation challenges, measurement uncertainties, and borderline cases. The approach facilitates clear criteria for species assignment while quantifying confidence and incorporating caveats, thereby enhancing analytical rigor and reducing misclassification risk. The decision pathway progresses through the following sequential steps:

- (i) Step 1: Primary call (bulk XRF R)  $R < 0.0033 \Rightarrow \text{Narwhal}, R > 0.0033 \Rightarrow \text{Walrus}.$
- (ii) Step 2: Boundary & red-flag handling If  $|R-R_0| \le 0.1R_0$  or any preservation/measurement red flag is present (e.g., Raman strong fluorescence + weak organics; SEM fissures/secondary fills; XRD peak broadening inconsistent with layer; anomalous oxide totals), then proceed to Step 3.
- (iii) Step 3: Secondary ratio & supportive cues Evaluate  $R_2 = \text{Mg/Na}$  (narwhal-leaning if < 0.75; walrus-leaning if > 0.75), together with XRD CI (with layer), Raman  $\nu_1$  width/amide presence, and SEM/FFT anisotropy metric A.
- (iv) Step 4: Composite decision

  Fuse the above using the MCDA/weighted-sum score in §4.6.3; report class, confidence, and any caveats.

#### **Computation of the Composite Decision Score (expanded)**

#### Feature extraction and normalization

The composite decision score is derived from heterogeneous physicochemical features that are first normalized into bounded, sigmoid-based mappings. Elemental ratios are expressed as signed log-distance metrics relative to reference thresholds, providing chemically robust discriminants. Crystallographic indices from XRD are converted to layer-specific scores to account for structural heterogeneity, while Raman-derived proxies integrate mineral crystallinity and organic content with baseline correction. Morphological anisotropy, quantified from SEM Fourier spectra, is further mapped into a walrus-leaning score to capture textural bias. These normalized features form the basis

ISSN's 0869 profit fusion into a unified decision metric. To operationalize this framework, each modality was formalized into a normalized feature score as follows:

### (a) Primary & secondary ratios

 $R = \text{Al}_2 \text{O}_3/\text{P}_2 \text{O}_5$ . Signed distance to threshold:  $d_R = \log_{10}(R/R_0)$ . Smooth walrusleaning score  $s_R = \sigma(d_R/\tau_R)$ , default  $\tau_R = 0.05$  (log units).

$$R_2 = {
m Mg/Na}$$
.  $d_{R_2} = {
m log_{10}}(R_2/0.75)$ , with  $s_{R_2} = \sigma(d_{R_2}/\tau_{R_2})$ , default  $\tau_{R_2} = 0.06$ .

#### (b) XRD Person CI (layer-aware)

Map CI to a walrus-leaning score  $s_{CI} \in [0,1]$ :

Inner dentin:  $s_{CI} = \sigma((CI - 3.5)/0.3)$ .

Cortical:  $s_{CI} = \sigma((1.7 - CI)/0.2)$ .

Layer unknown: use a wider, symmetric mapping centered near  $\sim 2.0$  to downweight ambiguity.

# (c) Raman proxy (crystallinity + organics)

Compute instrument-corrected FWHM<sub> $\nu_1$ </sub> at ~ 961 cm<sup>-1</sup>,

define  $CI_{Raman} = 1/FWHM_{\nu_1}$  and a normalized amide intensity  $I_{amide}$ . Combine into

$$z_{\rm Ra} = \alpha \cdot \frac{{
m CI}_{
m Raman} - \mu_{
m N}}{\sigma_{
m N}} - (1 - \alpha) \cdot \frac{I_{
m amide,ref} - I_{
m amide}}{I_{
m amide,ref}}, \alpha = 0.6,$$

with  $s_{\text{Raman}} = \sigma(z_{\text{Ra}}/1.0)$ . If strong fluorescence/poor baseline is detected, **clip**  $s_{\text{Raman}} = 0.5$  (uninformative).

## (d) SEM/FFT anisotropy

From 2-D FFT angular power  $P(\theta)$ , define

$$A = \frac{\max P(\theta) - \min P(\theta)}{\sum_{\theta} P(\theta)}.$$

ISSN: 0369-8963 Map "greater anisotropy  $\rightarrow$  narwhal" to  $s_{\text{SEM}} = 1 - \sigma((A_0 - A)/\tau_A)$  (defaults  $A_0 = 0.15$ ,  $\tau_A = 0.03$ ).

For fusion, convert to walrus-leaning as  $s_{\text{SEM}}^{(W)} = 1 - s_{\text{SEM}}$ .

# MCDA / Weighted-Sum (operational default)

The integration of modality-specific scores was implemented through a multi-criteria decision analysis (MCDA) approach, adopting a weighted-sum model as the operational default. Within this framework, each feature was first normalized to a walrus-leaning score ( $si \in [0,1]s_i \in [0,1]$ ), thereby ensuring scale invariance and direct comparability across heterogeneous descriptors. The assignment of relative weights was guided by both the robustness and discriminative capacity of individual modalities, with elemental ratios prioritized as the primary determinants, while crystallographic, spectroscopic, and morphological indices were incorporated as secondary modifiers. This weighting strategy ensures that chemically decisive features exert the greatest influence on the outcome, while structural and textural attributes provide complementary refinement. To operationalize this scheme, all modalities were constrained to yield normalized scores  $s_i \in [0,1]$  with SEM anisotropy expressed in its walrus-leaning form  $s_{\text{SEM}}^{(W)}$ . The recommended weights of robustness and separability are;

$$w_R = 0.60, w_{R_2} = 0.15, w_{CI} = 0.15, w_{Raman} = 0.05, w_{SEM} = 0.05, \sum_{i=1}^{N} w_{i} = 1.$$

The overall composite walrus score is then defined as the weighted sum of the individual normalized contributions:

$$S = \sum_{i} w_{i} s_{i}.$$

#### **Decision & confidence.**

Classification outcomes were defined on the basis of the composite score S, with assignments made according to fixed thresholds: specimens were designated as "walrus" when  $S\geq 0.50$ , "narwhal" when S<0.50, and "borderline" when  $0.45\leq S\leq 0.55$ . To quantify decision reliability, a continuous confidence index was introduced as  $C = |S - 0.5|/0.5 \in [0,1]$ , yielding values within [0,1], where higher values denote stronger separation from the decision boundary. To ensure robustness, a dominance rule was implemented such that the primary elemental ratio  $s_R$  supersedes the composite outcome when highly discriminative (i.e.,  $s_R\geq 0.95$  or  $s_R\leq 0.05$ , thereby preventing spurious reclassification by secondary features.

# ISDEM Ster Shafer (DS) evidence theory (for missing/weak evidence)

To accommodate cases of missing or weak evidence, decision support was extended using Dempster–Shafer (DS) evidence theory. For each modality, basic probability masses  $m_i(\{W\}), m_i(\{N\}), m_i(\Omega)$  were assigned based on the signed distance to the decision threshold. For the primary ratio R, the normalized distance was defined as;

$$\Delta_R = \frac{|d_R|}{\tau_R}, \eta_R = \min(1, \Delta_R/4), m_R(\{W\}) = \eta_R \, \mathbf{1}_{(R>R_0)}, m_R(\{N\}) = \eta_R \, \mathbf{1}_{(R$$

where  $\Omega$ ={W,N} denotes the frame of discernment. Evidence across modalities was subsequently combined using Dempster's rule to compute the belief function *Bel* and the conflict measure K. To ensure reliability, outcomes were flagged as *borderline* when either the conflict exceeded K>0.6K > 0.6K>0.6 or the difference in belief values fell below 0.1, with such cases escalated for higher-level evaluation (see §4.6.4). When reported in parallel with the continuous confidence index C=|S-0.5|/0.5, the DS framework provides an additional evidential layer, strengthening interpretability and mitigating the impact of uncertainty in borderline classifications.

## **Uncertainty, Conflict Resolution, and Sensitivity**

Escalation procedures were invoked under conditions of low discriminative margin or data quality concerns, specifically when  $|R-R_0| \le 0.1$ , when preservation or measurement anomalies were flagged, when the MCDA score fell within the borderline interval ( $S \in [0.45, 0.55]$ , when DS conflict exceeded K>0.6K, or when chemical inconsistencies (e.g., abnormal oxide totals or extreme Mg/Na ratios) were observed. In such cases, raw data and instrument calibrations were re-examined, targeted measurements were reacquired, and both MCDA and DS frameworks were applied in parallel; if convergence was not achieved, the outcome was designated *Borderline—escalated* with an explicit rationale. Sensitivity analyses were conducted once per study to evaluate robustness. These included perturbation of the reference threshold  $R_0$  by  $\pm 5-10\%$ , systematic variation of the primary weight  $w_R \in [0.5, 0.7]$  with renormalization, modality ablation to assess dependence, and performance benchmarking against the R-only rule using accuracy and Cohen's  $\kappa$ . Additionally, results were stratified by inner versus cortical layers to ensure correct handling of the known bimodality in walrus crystallinity indices.

Volume 94, No. 5, 2025

Periodico di Mineralogia

ISSN: 0369-8963

# **Per-Specimen Reporting**

For each specimen, a standardized reporting template was employed to capture both primary measurements and derived decision metrics. First, the elemental ratio R and its log-margin M = $\log_{10}(R/R_0)$  were reported together with the corresponding primary classification. Second, secondary descriptors were documented, including the ratio R<sub>2</sub>, the XRD crystallinity index CI with explicit layer annotation (inner dentin vs cortical), Raman-derived observations (v1 width, amide intensity, fluorescence interference), and SEM anisotropy parameter A. Third, the composite score S and confidence index C were provided, with optional inclusion of Dempster-Shafer belief and conflict values when that framework was applied. Fourth, the overall status was indicated as Final or Borderline—escalated, together with the explicit reason for escalation. Finally, a concise one-line rationale was recorded to identify the decisive evidence that governed the outcome. This structured format ensures that both numerical evidence and interpretive judgments are explicitly documented, thereby enhancing transparency and reproducibility.

#### **Conclusions**

This study demonstrates that a multi-modal analytical strategy integrating XRF, SEM-EDX, XRD, Raman spectroscopy, and SEM-FFT anisotropy provides a robust and reproducible framework for species-level discrimination of walrus and narwhal tusks. Bulk XRF-derived elemental ratios, particularly the Al<sub>2</sub>O<sub>3</sub>/P<sub>2</sub>O<sub>5</sub> threshold, emerged as the most decisive discriminator, achieving zero misclassification within the examined dataset. SEM-EDX and supplementary Mg/Na ratios, while partially overlapping, offered additional discriminatory strength in ambiguous cases. Raman and SEM data further resolved preservation state and microstructural organization, highlighting the contrast between crystalline, anisotropic narwhal dentin and isotropic, heterogeneous walrus dentin. XRDderived crystallinity indices reinforced these findings, revealing tightly clustered values in narwhal specimens and bimodal distributions in walrus tusks, consistent with anatomical layering and environmental exposure.

By formalizing these heterogeneous descriptors into a structured decision pathway supported by MCDA weighting and Dempster-Shafer evidence theory, this work establishes transparent classification criteria and a standardized reporting protocol. The proposed per-specimen template, documenting both primary ratios and secondary indices alongside composite scores, confidence, and rationale, ensures methodological rigor, traceability, and reproducibility across studies. Importantly, the convergence of multiple lines of evidence underscores the reliability of non-destructive screening

## Acknowledgements

The authors gratefully acknowledge Associate Professor Dr. Azimah Hussin for her invaluable guidance and sustained support throughout the course of this research. Sincere thanks are also extended to the anonymous donors from indigenous communities in the Russian Far East for generously providing walrus and narwhal tusk specimens. The Faculty of Science and Technology, Universiti Kebangsaan Malaysia, together with collaborating external laboratories, are acknowledged for their technical assistance and access to instrumentation. Finally, the authors express deep appreciation to Zhong Songyang, Yin Shiwei, and Guo Ye, as well as to family and friends, for their unwavering encouragement and moral support.

Periodico di Mineralogia ISSN: 0369-8963

#### References

- Dąsal, M., Smakosz, A., Kurzyna, W., & Rudko, M. (2021). "unicorn horn" drugs in the medical and pharmaceutical culture of europe. In *Farmacja Polska* (Vol. 77, Issue 2, pp. 84–94). Polish Pharmaceutical Society. https://doi.org/10.32383/farmpol/135093
- Edwards, H. G. M., & O'connor\*, S. (2012). Archaeological Ivories: A Challenge for Analytical Raman Spectroscopy. In *Analytical Archaeometry* (pp. 449–467). The Royal Society of Chemistry. https://doi.org/10.1039/9781849732741-00449
- ENGEL, W., GENNARI, R. F., FERREIRA, C., & RIZZUTTO, M. (2022). *IVORY CHARACTERIZATION USING PORTABLE VIBRATIONAL SPECTROMETRY*. 1–4. https://doi.org/10.48141/sbjchem.21scon.40\_abstract\_engel.pdf
- Etcheverry, S. B., Apella, M. C., & Baran, E. J. (n.d.). A Model Study of the Incorporation of Vanadium in Bone.
- Hemer, K. A., Willmott, H., Evans, J. E., & Buckley, M. (2023). Ivory from early Anglo-Saxon burials in Lincolnshire

   A biomolecular study. *Journal of Archaeological Science: Reports*, 49.

  https://doi.org/10.1016/j.jasrep.2023.103943
- Hoelzig, H., Muenster, T., Blanke, S., Kloess, G., Garmasukis, R., & Koenig, A. (2020). Ivory vs. osseous ivory substitutes—Non-invasive diffractometric discrimination. *Forensic Science International*, *308*. https://doi.org/10.1016/j.forsciint.2020.110159
- Kiladze, A. B., & Chernova, O. F. (2018). Data on the angular characteristics of the spiral structure of the narwhal tusk. *Data in Brief*, 20, 1700–1703. https://doi.org/10.1016/j.dib.2018.09.029
- Kinney, J. H., Balooch, M., Marshall, G. W., & Marshall, S. J. (1999). *Archives of Oral Biology A Micromechanics Model of the Elastic Properties of Human Dentin*.
- Lambert, J. B., & Poinar, G. O. (2002). Amber: The organic gemstone. *Accounts of Chemical Research*, *35*(8), 628–636. https://doi.org/10.1021/ar0001970
- Locke, M. (2008). Structure of ivory. Journal of Morphology, 269(4). https://doi.org/10.1002/jmor.10585
- Madupalli, H., Pavan, B., & Tecklenburg, M. M. J. (2017). Carbonate substitution in the mineral component of bone: Discriminating the structural changes, simultaneously imposed by carbonate in A and B sites of apatite. *Journal of Solid State Chemistry*, 255, 27–35. https://doi.org/10.1016/j.jssc.2017.07.025
- Manjunath, B. S. (1996). Texture features for browsing and retrieval of image data. *IEEE Transactions on Pattern Analysis and Machine Intelligence*, 18(8), 837–842. https://doi.org/10.1109/34.531803
- McLellan, M. J., Carrothers, K. L., & Spicer, A. M. (2022a). Investigating the utility of a handheld X-ray fluorescence (XRF) device as a field test for suspected ivory. *Forensic Science International: Animals and Environments*, 2. https://doi.org/10.1016/j.fsiae.2022.100041
- McLellan, M. J., Carrothers, K. L., & Spicer, A. M. (2022b). Investigating the utility of a handheld X-ray fluorescence (XRF) device as a field test for suspected ivory. *Forensic Science International: Animals and Environments*, 2. https://doi.org/10.1016/j.fsiae.2022.100041
- Morris, M. D., & Mandair, G. S. (2011). Raman assessment of bone quality. *Clinical Orthopaedics and Related Research*, 469(8), 2160–2169. https://doi.org/10.1007/s11999-010-1692-y
- Nazhvani, D. D. (2019). Ultrastructural and Chemical Composition of Dentin and Enamel in Lab Animals. *J Dent Shiraz Univ Med Sci*, 20(3), 178–183. https://doi.org/10.30476/DENTJODS.2019.44912
- Nganvongpanit, K., Buddhachat, K., Klinhom, S., Kaewmong, P., Thitaram, C., & Mahakkanukrauh, P. (2016). Determining comparative elemental profile using handheld X-ray fluorescence in humans, elephants, dogs, and dolphins: Preliminary study for species identification. *Forensic Science International*, 263, 101–106. https://doi.org/10.1016/j.forsciint.2016.03.056

ISS Nan October 2016; K., Buddhachat, K., Piboon, P., & Klinhom, S. (2016). The Distribution of Elements in 48 Canine Compact Bone Types Using Handheld X-Ray Fluorescence. *Biological Trace Element Research*, 174(1), 93–104. https://doi.org/10.1007/s12011-016-0698-z

- Person, A., Bocherens, H., Saliège, J. F., Paris, F., Zeitoun, V., & Gérard, M. (1995). Early Diagenetic Evolution of Bone Phosphate: An X-ray Diffractometry Analysis. *Journal of Archaeological Science*, 22(2). https://doi.org/10.1006/jasc.1995.0023
- Sastri, C. S., Banerjee, A., Sauvage, T., Courtois, B., & Schuhmacher, T. (2013). Fluorine determination in different types of ivory by PIGE technique. *Journal of Radioanalytical and Nuclear Chemistry*, 298(1), 311–315. https://doi.org/10.1007/s10967-012-2410-x
- Sims, M. E., Baker, B. W., & Hoesch, R. M. (2011). Tusk or Bone? An Example of Ivory Substitute in the Wildlife Trade. *Ethnobiology Letters*, 2. https://doi.org/10.14237/ebl.2.2011.27
- Smičiklas, I., Dimović, S., Šljivić, M., Plećaš, I., Lončar, B., & Mitrić, M. (2010). Resource recovery of animal bones: Study on sorptive properties and mechanism for Sr2+ ions. *Journal of Nuclear Materials*, 400(1), 15–24. https://doi.org/10.1016/j.jnucmat.2010.02.004
- Tranchant, L., Müller, K., Lemasson, Q., Pichon, L., Schöder, S., Conard, N. J., & Reiche, I. (2023). Improved discrimination of biogenic and diagenetic elements in Palaeolithic mammoth ivory and bone from Hohle Fels Cave in the Swabian Jura of Southwestern Germany. *Quaternary International*, 660, 4–12. https://doi.org/10.1016/j.quaint.2023.02.006
- Unal, M., Ahmed, R., Mahadevan-Jansen, A., & Nyman, J. S. (2021). Compositional assessment of bone by Raman spectroscopy. In *Analyst* (Vol. 146, Issue 24, pp. 7444–7470). Royal Society of Chemistry. https://doi.org/10.1039/d1an01560e
- Xiang, S., Jiang, L., Wang, Y., Li, S., Jiang, L., Wang, N., Zhu, L., Zhao, L., & Hong, J. (2024). Research on the microstructure and water effect of excavated ivory from sacrificial pit No.7 at the Sanxingdui Ruins. *Heritage Science*, 12(1). https://doi.org/10.1186/s40494-024-01531-8
- Xiao, F. (2017). A novel evidence theory and fuzzy preference approach-based multi-sensor data fusion technique for fault diagnosis. *Sensors (Switzerland)*, 17(11). https://doi.org/10.3390/s17112504

ISSN: 0369-8963

Narwhal Tusk (N3)

Walrus Tusk (W8.)

Walrus Tusk (W10)

Figure 1 Comparison of narwhal (N3, N5) and walrus (W8, W10) tusks. Narwhal ivory is smooth, pale, and fine-textured, while walrus ivory is marbled, mottled, and structurally varied highlighting key traits for identification

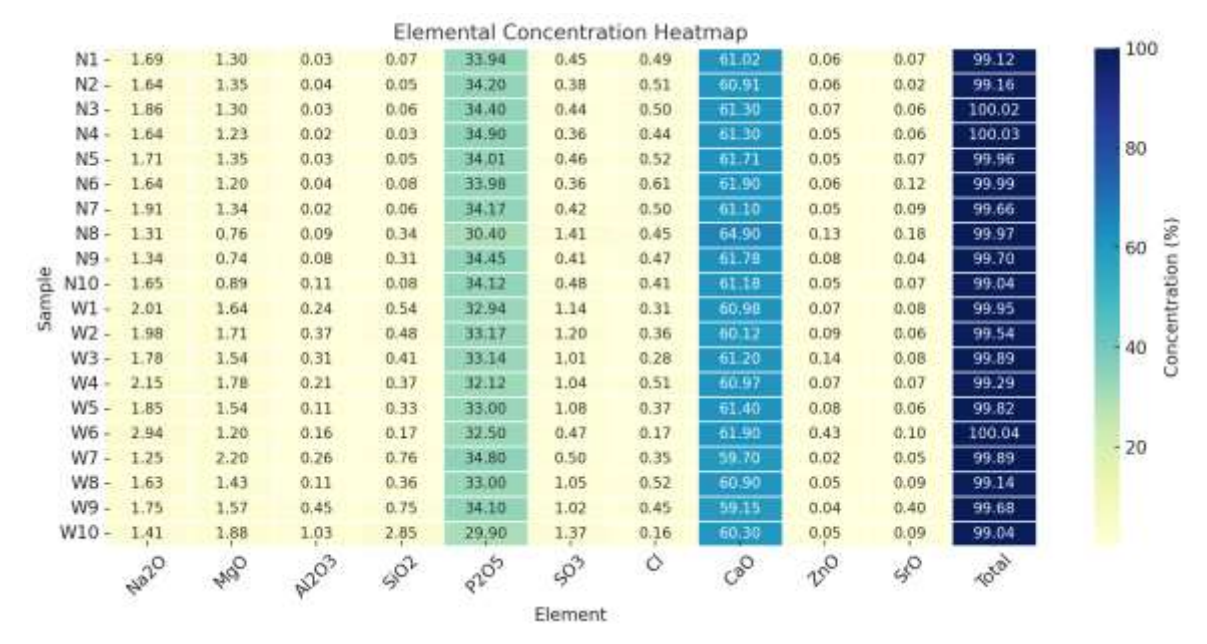


Figure 2 XRF elemental concentration heatmap of the samples

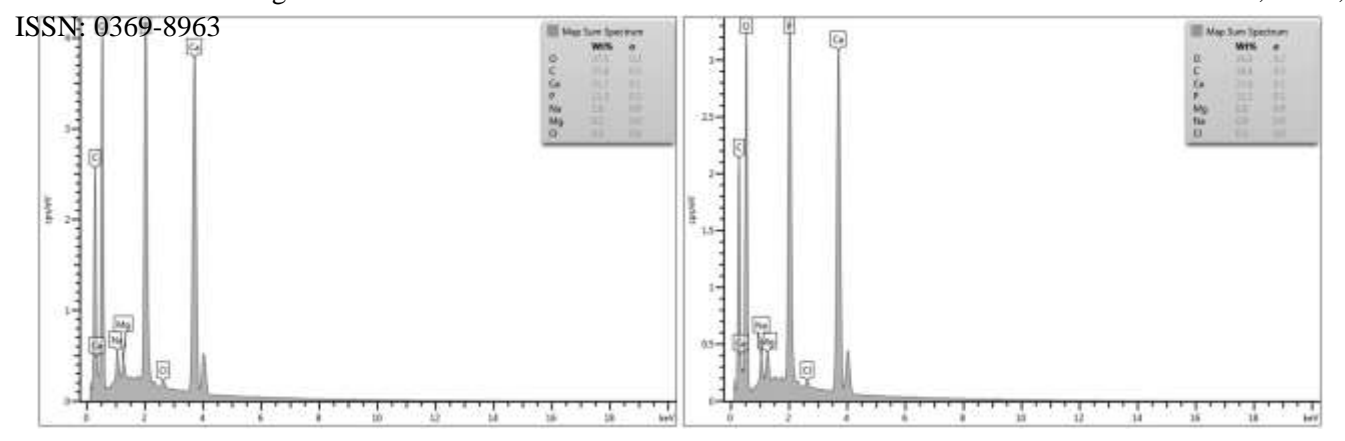


Figure 3 SEM-EDX Spectrum of Representative Sample N6(left) and W9(right)

Table 1 Comparative EDX Quantitative Results for Narwhal and Walrus Tusk

Element	Narwhal Tooth (EDX wt %)	Walrus Tooth (EDX wt %)	Difference (Walrus – Narwhal)
О	$37.5 \pm 0.2$	$36.8 \pm 0.2$	-0.7
С	$27.8 \pm 0.3$	$28.4 \pm 0.3$	+0.6
Ca	$21.7 \pm 0.1$	$21.8 \pm 0.1$	+0.1
P	$11.3 \pm 0.1$	$11.1 \pm 0.1$	-0.2
Na	$1.0\pm0.0$	$0.8 \pm 0.0$	-0.2
Mg	$0.5 \pm 0.0$	$0.8 \pm 0.0$	+0.3
Cl	$0.3 \pm 0.0$	$0.3 \pm 0.0$	0.0

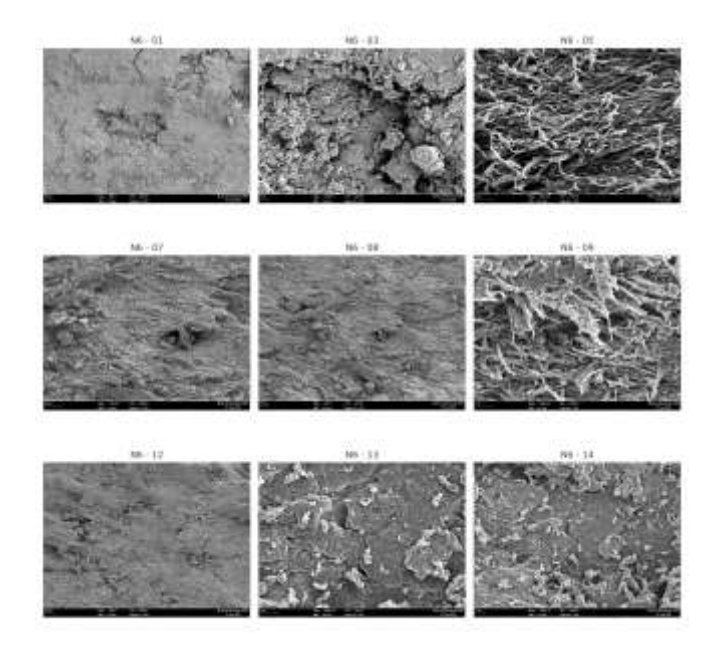


Figure 4 Representative SEM Micrographs of Sample Group N6

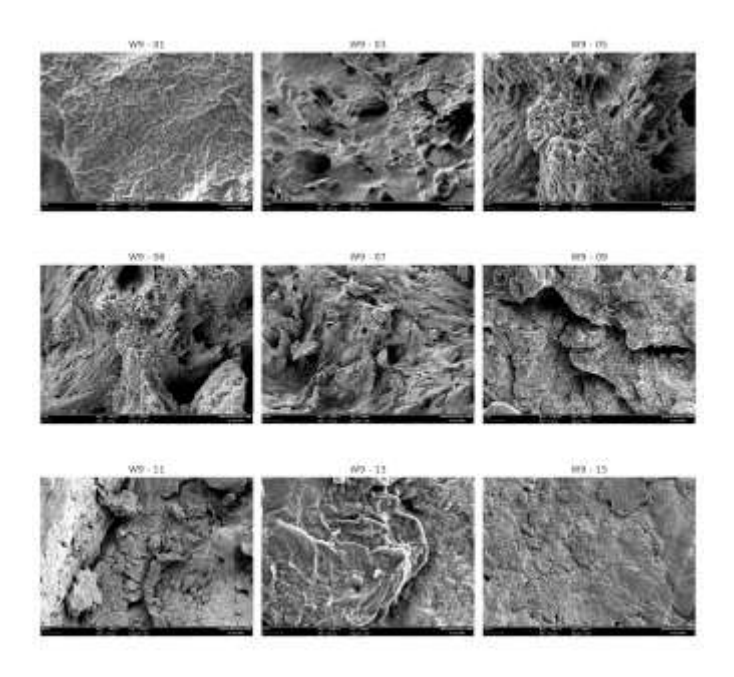


Figure 5 Representative SEM Micrographs of Sample Group W9

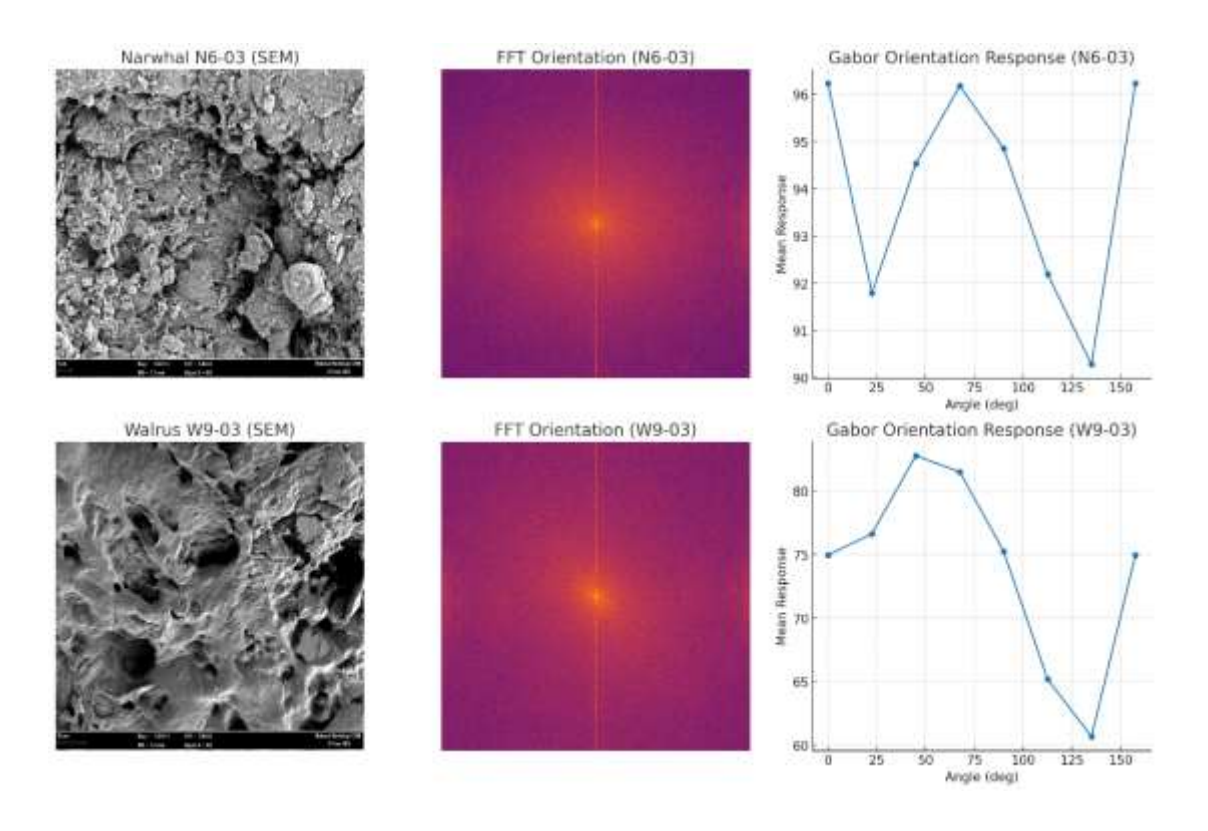


Figure 6 Gabor Orientation Response (W9-03 and N6-03)

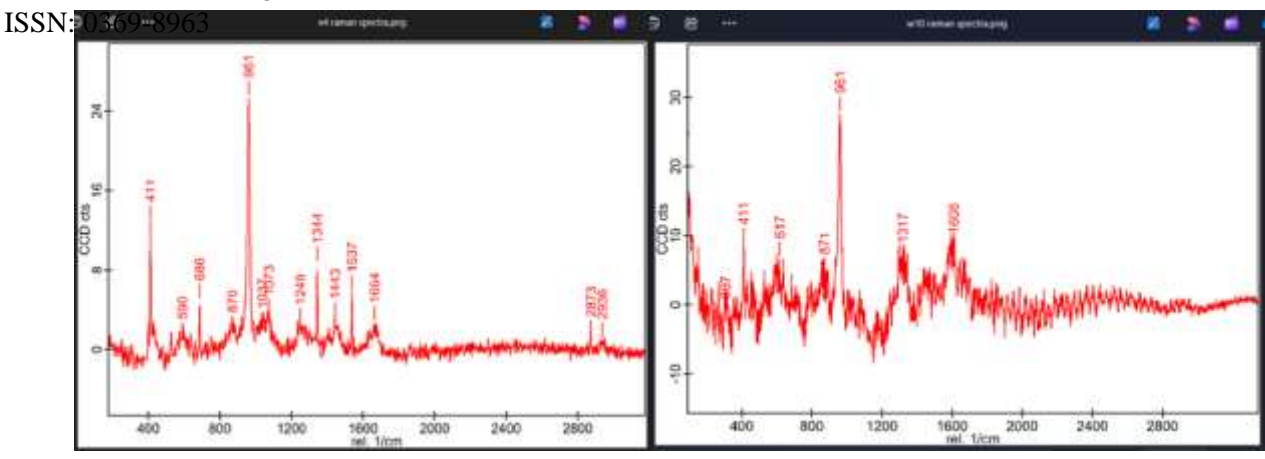


Figure 7 Raman Spectra of Representative Narwhal (N4) and Walrus (W10) Tusks Samples

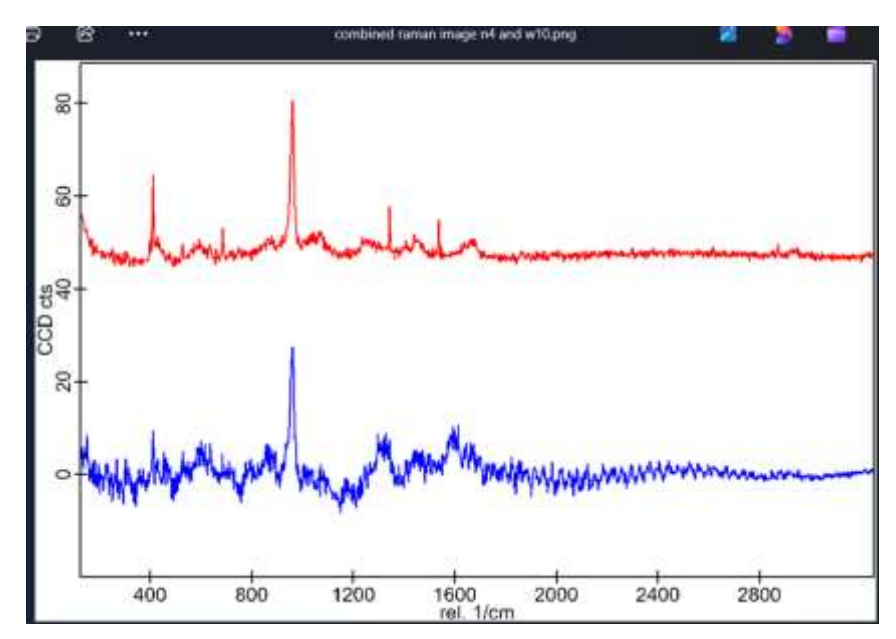
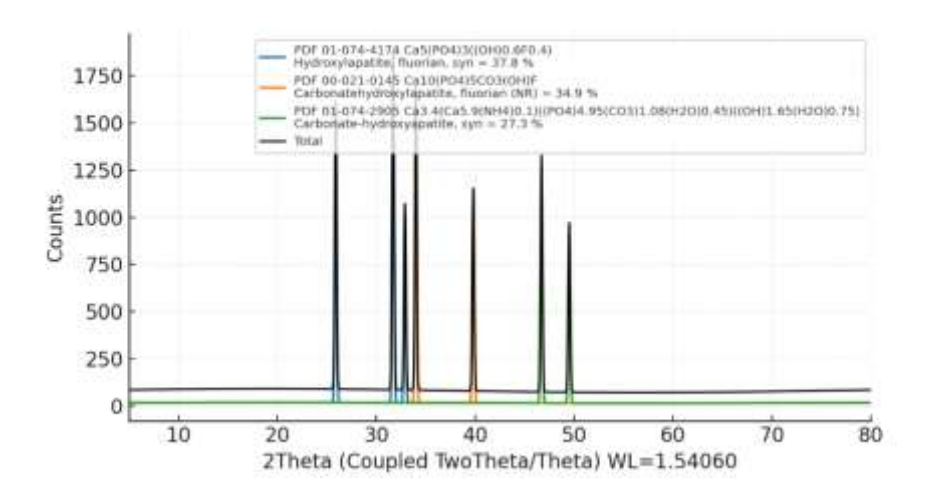


Figure 8 Combined Raman spectra of narwhal tusk (N4, red) and walrus tusk (W10, blue)





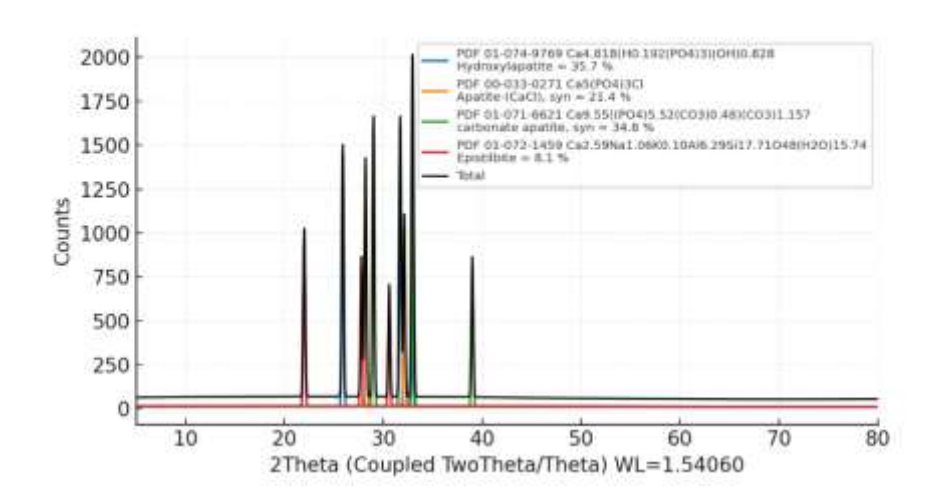


Figure 9 Comparative XRD patterns of narwhal tusk (N6) and walrus tusk (W9)

Periodico di Mineralogia ISSN: 0369-8963

Table 3 Crystallinity Index (CI) — Results

Sample	CI	
N1	2.13	
N2	2.49	
N3	1.85	
N4	2.57	
N5	2.05	
N6	1.85	
N7	1.87	
N8	1.84	
N9	1.96	
W1	4.42	
W2	5.1	
W3	1.21	
W4	0.67	
W5	0.99	
W6	0.81	
W7	0.89	
W8	0.93	
W9	1.35	